NANOSYSTEMS:
PHYSICS, CHEMISTRY, MATHEMATICS

Nadeina K.A., et al. *Nanosystems: Phys. Chem. Math.*, 2024, **15** (6), 837–854.
http://nanojournal.ifmo.ru
DOI 10.17586/2220-8054-2024-15-6-837-854

Original article

Granular Ni–Mo–W bulk hydrotreating catalyst: the effects from precursor calcination

Ksenia A. Nadeina, Yuliya V. Vatutina, Polina P. Mukhacheva, Sergey V. Budukva, Irina G. Danilova, Vera P. Pakharukova, Evgeniy Yu. Gerasimov, Maxim A. Panafidin, Oleg V. Klimov

Boreskov Institute of Catalysis SB RAS, Pr. Lavrentieva 5, 630090 Novosibirsk, Russia

Corresponding author: Ksenia A. Nadeina, lakmallow@catalysis.ru

PACS 81.05.-t, 81.05.Rm, 81.20.-n, 81.40.-z

ABSTRACT This paper presents a study on the effect of the Ni–Mo–W precursor calcination (300, 450 and 500 °C) on properties of granulated bulk Ni–Mo–W catalysts. The Ni–Mo–W precursor and bulk catalysts were studied by XRD, nitrogen adsorption-desorption method, CHNS analysis, thermal analysis, Raman spectroscopy, UV-Vis DR spectroscopy, HRTEM and XPS. It is shown that the increase in calcination temperature of the precursor to 500 °C leads to stepwise decomposition of citric acid, transformation of active metals and re-structurization of the samples. Active metals in sulfide catalysts are present in the bulk mixed or individual sulfides and interact with alumina binder to form "NiMoS-like" sulfide phase. Increased crystallinity of the precursor results in the enlargement of bulk nickel particles, capsulation of Mo and W and their rounding by Ni atoms. Catalysts testing in hydrotreatment of SRVGO demonstrates that the best choice of temperature regimes is 300 °C for the precursor.

KEYWORDS bulk catalyst, NiMoW, calcination, HDS, HDN

ACKNOWLEDGEMENTS The study was funded by the Russian Science Foundation according to the research project No. 22-73-10144 (https://rscf.ru/en/project/22-73-10144/).

FOR CITATION Nadeina K.A., Vatutina Yu.V., Mukhacheva P.P., Budukva S.V., Danilova I.G., Pakharukova V.P., Gerasimov E.Yu., Panafidin M.A., Klimov O.V. Granular Ni–Mo–W bulk hydrotreating catalyst: the effects from precursor calcination. *Nanosystems: Phys. Chem. Math.*, 2024, **15** (6), 837–854.

1. Introduction

Hydroprocessing catalysts are attracting constant interest from scientists working in catalysts development. It is caused by the constantly emerging requirements for the resulting fuels and heavy feedstocks of secondary processing and, consequently, the requirements for the catalytic action of the corresponding catalysts.

Hydrotreating (HDT) catalysts used in industrial units can be supported or bulk systems. The main similarity between them is the nature of active metals. Typically, Co or Ni are used in the pair with Mo or W [1, 2]. Combination of these metals in a catalyst followed by their transition in active sulfide phase provides high activity in target hydrotreating reactions.

The structure of active component of hydrotreating catalysts is sufficiently well determined, if bimetallic NiMo or CoMo catalysts are considered. According to Topsøe et al. [3], the active component of such CoMo systems consists of molybdenum sulfide particles being decorated with the promotor atom. However, the formation of Co–Mo–S phase is observed at Co/Mo ratios < 0.4, while greater Co contents result in the formation of Co–Mo–S phase and individual CoxSy sulfides. In general, NiMo catalysts have similar structure of Ni–Mo–S phase [4].

When adding the third element, Co/Ni or Mo/W, a synergetic effect can be observed. It is known that Ni–Mo and Co–Mo catalysts have better hydrogenolysis activity, while Ni–W catalyst is stronger in hydrogenation. Combining these advantages of bimetallic catalysts, Albemarle, ExxonMobil, and the Nippon Ketjen Corporation jointly developed the bulk catalyst (NEBULA) [5, 6], which presents of Ni–Mo–W component and demonstrates a breakthrough catalytic activity. The preparation procedure of NEBULA is know-how of the producer company. That is why, numerous investigations in this field are carried out by the catalysts developers to understand the nature of Ni–Mo–W catalysts and to create new high-active bulk catalysts.

Obviously, the presence of three different metals in the Ni–Mo–W system significantly increases the complexity of the system. Density functional theory (DFT) calculations confirmed the formation of synergetic effect of the addition of Ni to Mo–W–S system [7]. Moreover, it is shown that the best HDT catalysts must exhibit sulfur metal bond energies close to $NiMo_{0.5}W_{0.5}S_2$ system, meaning between NiMoS and NiWS ones. The data in [8] shows that the surface of NiMoW catalysts is easily formed comparing to bimetallic systems and the edge of NiMoW particle exhibits the highest occupation density of d-type states near the Fermi level. The equilibrium morphologies of the sulfide particles of the active component CoMoS or NiMoS phase are hexagonal or trigonal particles, according to DFT calculations [9]. According to the calculations, the shape of the main particle is close to the bimetallic one. In the case of the supported system, the

active component particles were highly dispersed, highly reducible, and highly sulfidable W/Mo species, that provided the formation of $W_xMo_{1-x}S_2$ phases with increased capability for accommodating NiS_x at the edges of sulfide slabs [10].

For the bulk NiMoW catalysts, the establishment of the composition of active particles is complicated by the absence of the support, which can unify the active phase, as well as the use of numerous preparation techniques and conditions of activation procedures. Moreover, some preparation procedures can lead to the formation of the bulk hydrodesulfurization (HDS) catalysts with low atom efficiency and intrinsic activity due to the large amount of unused active sites embedded in the bulk catalyst, leading to the limitation of the practical application in HDS process [11, 12]. Therefore, optimization of bulk catalyst preparation is a complicated task.

In our previous research, it is shown that among all widely used preparation techniques for the bulk NiMoW catalysts, the best method includes the synthesis of the active metals precursor in the solution followed by spray drying [13]. It allows a synthesis of a set of compounds with high activity in HDS and hydrodenitrogenation (HDN) reactions. We found that the more preferred calcination temperature of the granulated catalyst prepared by the above-mentioned method is 300 °C [14]. However, the question on calcination of the precursor, which would define final structure of the oxide system before calcination, still arises.

For example, Wang et al. [15] used a surfactant-assisted co-precipitation method from the starting materials including basic nickel carbonate followed by a sulfidation process to obtain the final Ni–Mo–W sulfide catalyst without previous calcination of the precursor. The given data showed the formation of hydrotalcite-like structures, where Mo–W–S particles are located between Ni_7S_6 layers that significantly improves promotion effect from Ni.

On the contrary, in a number of works and patents, calcination temperature of bulk catalysts is usually in the range of 300 – 400 °C, however, there are no arguments for the chosen temperatures [12, 16, 17]. The report [18] demonstrates the data on the influence of thermal treatment at 250, 350, 450, 550 and 650 °C of a bulk NiMo catalyst being prepared by coprecipitation method on HDS activity of DBT. It is shown that the catalyst calcined at 350 °C is the most active in HDS than other samples. Similar results are shown in the report [19] for bimetallic NiMo catalysts, where calcination procedure is carried out under hydrogen or nitrogen atmosphere in the temperature range from 350 to 600 °C. It is shown that the best activity is achieved at calcination temperature of 400 °C. However, hydrothermal synthesis procedure of the precursor used in the above-mentioned papers, as well as calcination conditions, are not optimal for industrial application. Moreover, these works do not consider the necessity to use binding agent, such as pseudoboehmite, for granulation. It should also significantly influence the formation of the oxide active component precursor and then catalysts activity.

In the present work, we tried to clarify in detail the effect of calcination temperature on the NiMoW precursor for the bulk hydrotreating catalysts. The work focuses on the preparation of granulated system and, therefore, on the use of pseudoboehmite as a binding agent and its interaction with active component in the bulk system. Catalysts activity was assessed in a real feedstock hydrotreating.

2. Experimental

2.1. Preparation of catalysts

NiMoW precursor was synthesized by dissolution of nickel hydroxide, ammonium heptamolybdate and ammonium metatungstate with citric acid using the procedure described in [20]. Citric acid was dissolved in a distilled water under stirring at 70 °C. Then nickel hydroxide was added to the solution followed by complete dissolution and preparation of green transparent solution. Ammonium heptamolybdate and ammonium metatungstate were added to the green solution and it was stirred until complete dissolution. Molar ratio of Ni/Mo/W was 1/0.5/0.5. The obtained solution with the precursor was spray dried to prepare NiMoW powder. Then, the NiMoW powder was calcined at 300, 400, 450 or 500 °C in air flow. It should be emphasized that after studies by XRD and TGA the NiMoW sample calcined at 400 °C was not chosen for other investigations.

Granulated NiMoW catalysts were prepared by the following procedure. First, a dry mixing of the powder of the NiMoW precursor and a binder (pseudoboehmite) was carried out to obtain a kneading paste. A pseudoboehmite powder (SSA – 241 m^2/g, V_p – 0.6 cm^3/g, CSR: [100] – 14.5 nm, [010] – 4.0 nm, [001] – 11.5 nm) was synthesized by the procedure described in [21]. The weight ratio of pseudoboehmite and NiMoW precursor was 0.6. Then, an aqueous solution of plasticizing agent (nitric acid) was prepared. The amount of nitric acid was calculated from molar ratio of $HNO_3/Al_2O_3 = 0.07$. The obtained solution was added to the mix of powders and stirred to obtain plastic paste. The paste was extruded via fluoroplastic spinneret with trilobe holes of 1.3 ± 0.1 mm. The extrudate was then dried at 110 ± 10 °C and then calcined at 300 ± 10 °C.

2.2. Sulfiding and testing of catalysts

To assess catalysts activity in HDS and HDN reactions, catalysts were tested in hydrotreatment (HDT) of the real feedstock. Hydrotreatment of the real feedstock was carried out in a fixed-bed pilot unit using straight-run vacuum gas oil (SRVGO) (7080 ppm S and 958 ppm N). The 30 cm^3 of a catalyst sample was diluted with silicon carbide (0.1 – 0.2 mm) in a volume ratio of 1:2 and loaded in the isothermal zone of the reactor. Before testing, catalysts were sulfided in a liquid phase using the mixture of straight-run gasoil and dimethyl disulfide (20 g of DMDS per 1 l of straight-run gasoil).

Sulfidation of catalysts was carried out at 8.0 MPa, sulfidation mixture flow – 2 h^{-1} and volume ratio H_2/sulfidation mixture – 300 Nm^3/m^3 at 240 °C for 16 h and at 340 °C for 16 h. After sulfidation catalysts were tested in the following conditions: liquid hourly space velocity = 1.5 h^{-1}, H_2/feedstock = 600 Nm^3/m^3, $P = 8.0$ MPa, $T = 340$, 350 and 360 °C. Catalysts were tested for 48 h at each temperature. There were no liquid samples during first 24 h at each temperature. That period was marked as no steady state. Then, 4 liquid product samples were selected for analysis each 4 h. Content of nitrogen and sulfur in the feedstock and hydrotreating products was determined on Xplorer-NS Analyzer (TE Instruments).

2.3. Characterization methods

CHNS analysis was carried out on the analyzer VARIO EL CUBE according to ASTM D3176-15.

X-ray diffraction experiments in the transmitted light mode were carried out with MoKα radiation ($\lambda = 0.7093$ Å) at STOE STADI MP (STOE, Germany) installation using the detector MYTHEN2 1K. Measurements were carried out by scanning in the angles range 2 – 69° at 0.015° step at 2θ. The obtained data were analyzed to define average crystallite size. The size of coherent scattering region (CSR – D_{XRD}) was calculated from the width of diffraction peaks. Phase analysis was made using diffraction database ICDD PDF-2.

The textural properties of the catalysts were determined by nitrogen physisorption using an ASAP 2400 instrument (Micrometrics, USA). Prior to analysis, samples were subjected to a N_2 flow at 150 °C for 2 h. The Brunauer–Emmett–Teller method (BET) was used to calculate BET surface areas from the nitrogen uptakes at relative pressures ranging (P/P_0) from 0.05 to 0.30. The total pore volume was derived from the amount of nitrogen adsorbed at a relative pressure close to 1 (in practice, $P/P_0 = 0.995$). The pore size distribution was calculated by the Barrett–Joyner–Halenda (BJH) method using the desorption branch of the isotherm [22]. The uncertainty of the results was 10 %.

Sulfide catalysts were studied by X-ray photoelectron spectroscopy (XPS) on a SPECS photoelectron spectrometer using non-monochromatic MgKα radiation ($h\nu = 1253.6$ eV). The binding energy scale (E_b) was previously calibrated by the position of photoelectronic lines of core levels of gold, silver and copper: Au4$f_{7/2}$ – 84.0 eV, Ag3$d_{5/2}$ – 368.3 eV and Cu2$p_{3/2}$ – 932.7 eV, measured for corresponding metallic foils. Samples were applied to a double-sided conductive copper tape. The charging effect that occurs during electron photoemission was taken into account using the internal standard method, which used the Al2p line from aluminum in the support ($E_b = 74.5$ eV) [23]. In addition to the survey spectrum, high resolved spectral regions of elements being included to the samples were recorded. All obtained spectra were recorded at pass energy of 20 eV. The definition of a relative elements content on catalysts surface and a ratios of their atomic concentration were made from integral intensity of photoelectron lines being corrected by atomic sensitive factors [24].

Sulfide catalysts before reaction were studied by high-resolution transmission electron microscopy (HRTEM) to investigate their morphology and structure. For imaging in TEM and STEM modes, a ThemisZ two-corrector transmission electron microscope (USA, Thermo Fisher Scientific) with an accelerating voltage of 200 kV and a limiting resolution of 0.07 nm (TEM) and 0.06 nm (SEM) was used. The micrographs were recorded using a Ceta 16 CCD matrix (Thermo Fisher Scientific, USA). High-angle annular dark field (HAADF) technique was performed to evaluate distribution of active metals.

Thermal analysis of the catalysts was carried out using NETZSCH STA 449 Jupiter. A sample was loaded into corundum crucibles and placed in a chamber. An air flow rate was 30 ml/min. A sample was heated up to 600 °C at a rate of 10 °C/min. Experimental data was analyzed by the NETZSCH Proteus Thermal Analysis software.

UV-Vis diffuse reflectance spectra (UV-Vis DRS) of the catalysts in the oxide states were recorded on an UV-2501 PC Shimadzu spectrometer with an IRS-250A diffusion reflection attachment. The measurements were performed in a quartz cell (optical path length 2 mm) in air at room temperature using $BaSO_4$ as a reference.

Raman spectra of the catalysts in the oxide states were recorded with the use of a LabRAM HR spectrometer, Evolution, Horiba, equipped by a multichannel CCD detector, which was cooled by liquid nitrogen. The spectra were excited by a 633 nm He–Ne laser with a power of about 0.5 mW on the sample surface. The diameter of the laser light spot on the sample surface was about 2 μm. The scattering geometry was 180°. The spectrometer resolution was 2.4 cm^{-1}.

The structural properties of the samples were analyzed by Infrared (IR) spectroscopy using a KBr wafer technique (a typical wafer containing 1 wt. % of a sample). IR spectra were recorded on a Shimadzu IRTracer-100 spectrometer within the spectral range of 350 – 4000 cm^{-1} with a resolution of 2 cm^{-1}.

3. Results and discussion

3.1. Structure of NiMoW precursor after calcination at high temperatures

Before explanation of the data, which are given below for the precursor and catalysts, it would be better to justify the choice of the calcination temperature for the NiMoW precursor. The first point is based on the granulation of the catalysts. It is experimentally established that the NiMoW precursor has very poor plasticizing properties, when the calcination temperature is less than 300 °C. The second point is related to phase transitions seen in TG/DTG/DSC curves and XRD patterns.

The DTG curve (Fig. 1) of the NiMoW precursor contains specific features being characteristic for the decomposition of citrate ligands [25–27]. A weight loss at 50 – 150 °C can be assigned to the removal of adsorbed water and ammonia. A great weight loss (25 % of the total weight) is observed at 180 – 350 °C due to the citrate ligands decomposition to acetondicarboxylate compounds or oxycarbonate compounds [25, 28]. The decomposition of citrate complexes to carbon deposits occurs at ∼ 300 °C. It possibly explains poor plasticizing properties of the NiMoW powder. The weight loss over 400 – 600 °C is accompanied by a strong exo-effect, which is related to the oxidation of residual fragments of organic molecules and amorphous carbon, and to the formation of nickel, molybdenum and tungsten oxide compounds, and their phase transformation [29–31]. When the calcination temperature is higher than 300 °C, two areas can be pointed out: 400 – 450 °C and 500 – 550 °C. To choose calcination temperature in these two areas for further studies, the NiMoW precursors calcined at 300, 400, 450 and 500 °C were studied by XRD analysis (Fig. 2).

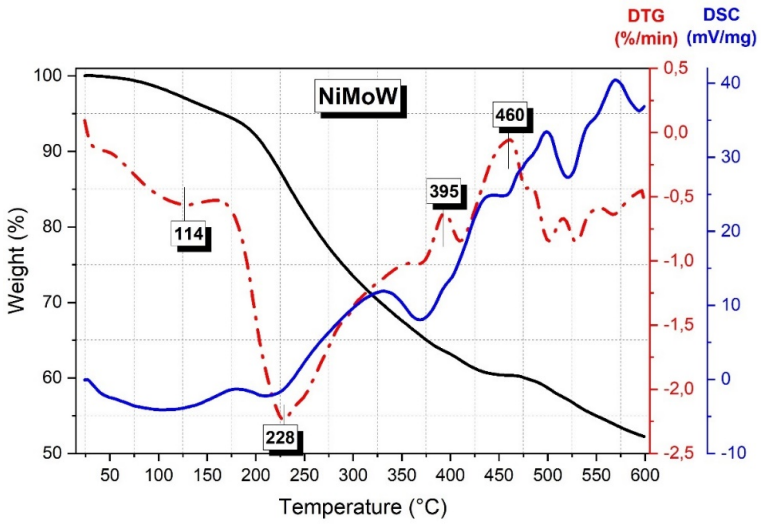

FIG. 1. TG and DTG curves of NiMoW precursor

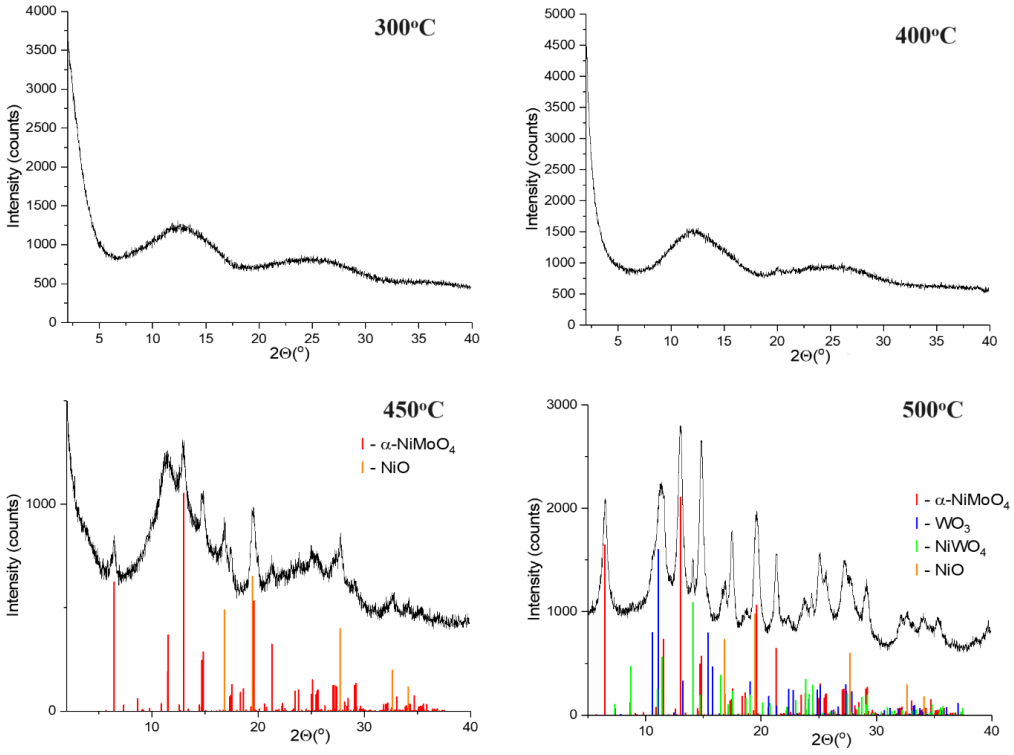

FIG. 2. XRD patterns of Ni–Mo–W precursor calcined at 300, 400, 450 and 500 °C

It is seen that only calcination at temperatures higher than 400 °C leads to the formation of crystal phases. Moreover, crystallinity of the samples calcined at 450 and 500 °C strongly changes. Then, we choose one of the X-ray amorphous samples, which were calcined at 300 °C, and two samples calcined at 450 and 500 °C for further studies.

3.1.1. NiMoW precursor calcined at 300 °C. As it is noted above, the XRD data of the precursor calcined at 300 °C does not show any crystal phases. On the contrary, the Raman spectrum (Fig. 3A) of the NiMoW sample calcined at 300 °C contains a set of bands in the range of 1100 – 1700 cm^{-1} with two intense poor resolved signals at 1360 and 1590 – 1600 cm^{-1} typical for most kinds of carbonaceous materials such as graphite, carbon black and soot. Considering calcination temperature, the peak at 1590 – 1600 cm^{-1} (G-band) can be assigned to graphitized coke, while the peaks at around 1360 cm^{-1} (D-band) can be due to disordered pseudographite deposits [32, 33]. The band at 1445 – 1465 cm^{-1} (D3-band) corresponds to the loss of aromatic bonding in a purely sp2 network [34]. The signal at 1250 – 1265 cm^{-1} corresponds to the Raman shift of C–H bond vibrations, while the shoulder at 1150 – 1200 cm^{-1} could be attributed to sp^2-sp^3 bonds or C–C and C=C stretching vibrations of polyene-like coke. In addition, a strong fluorescence background is detected in the sample calcined at 300 °C, probably caused by residual fragments of the organic matrix [35]. The observed features can indicate the effects from deposits of citric acid in the catalysts. A small signal at $\sim$ 220, 650 – 690 and $\sim$ 960 cm^{-1} can be assigned to bridged Mo–O–Mo and terminal M=O in polymolybdate-like structures [36].

The UV-Vis DR spectrum of NiMoW precursor (Fig. 4A) calcined at 300 °C represents a very intense broad signal in the region of 400 – 700 nm with the maximum at around 500 nm and shoulders at about 420 – 430, 350 – 360 and 280 – 300 nm. This set of bands may belong to π-π^* and n-π^* transitions of charged alkylated aromatics and polyaromatics with oxygen-containing substituents (the products of citric acid decomposition after calcinations) [37]. The absence of clearly defined bands of d-d transitions of Ni^{2+} ions may indicate shielding by a carbon matrix.

3.1.2. NiMoW precursors calcined at $>$ 450 °C. When calcination temperature is higher than 450 °C, XRD patterns contain peaks from α-$NiMoO_4$ (PDF#00-033-0948, $a = 9.509$, $b = 8.759$, $c = 7.667$ Å) with the average CSR size $D = 10$ nm (content prevails). Moreover, the precursor calcined at 450 °C contains NiO phase (PDF#00-047-1049,

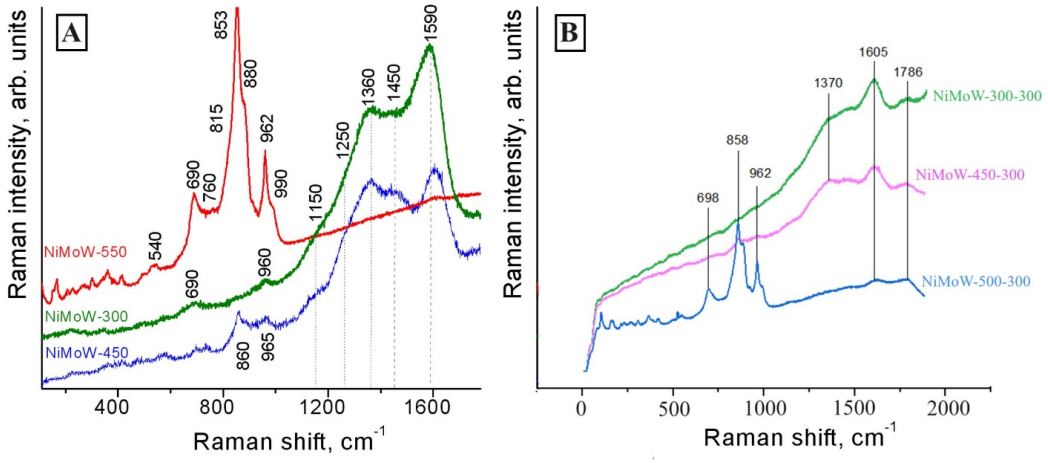

FIG. 3. Raman spectra of Ni–Mo–W precursor (A) and corresponding catalysts (B) calcined at 300, 450 and 500 °C

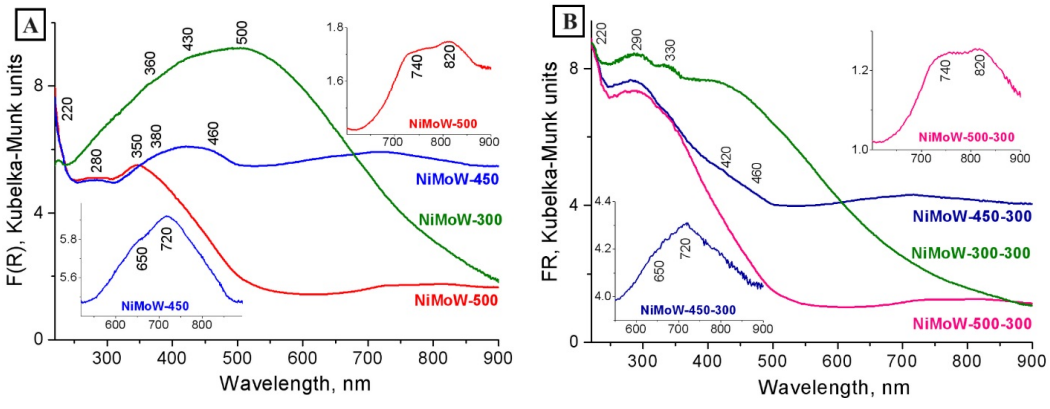

FIG. 4. UV-Vis DR spectra: A) Ni–Mo–W precursor calcined at 300, 450 and 500 °C; B) NiMoW–X-300 (where X = 300, 450 and 500 °C) catalysts. The insets show enlarged fragment of spectra

$a = b = c = 4.177$ Å) with $D = 10$ nm and with high probability highly dispersed WO_3 phase (PDF#00-033-1387), since there is an increase in the intensity near 11° at 2θ.

The set of bands in the Raman spectra (Fig. 3A) in the region of 1100 – 1700 cm^{-1} decreases in intensity and new peaks appear at about 540, 705, 740, 860 and 920 cm^{-1}. The band at 860 cm^{-1} can be attributed to W=O bonds in isolated WO_4 structures, while the signal at *ca.* 740 cm^{-1} is assigned to W=O bonds in isolated WO_6 structures [38]. The set of bands at 965, 920 and 705 cm^{-1} belongs to the MoO_6 symmetric stretch and corresponding MoO_6 asymmetric vibrations of bulk β-$NiMoO_4$ [36], while the band at 760 cm^{-1} is attributed to bridging Mo–O–Mo bond that confirms the presence of polymolybdate structures. The peak at about 540 cm^{-1} is typical for NiO.

Treatment at 450 °C is accompanied by the appearance of the intense peak at 720 nm with the shoulder at 650 nm in the UV-Vis DR spectra (Fig. 4A). This signal as well as the bands located at about 380 – 460 nm result from d-d transitions of Ni^{2+} ions hosted by octahedral sites in the dispersed NiO [39]. The n-π^* transitions in carboxylate substituents of the carbon matrix likely have an additional contribution to the adsorption in the 350 – 460 nm region and the increased background in the long wavelength region. The UV region of this spectrum contains three strong broad bands centered at 220, 280 and 350 nm, which could be assigned to $O^{2-} \rightarrow Mo^{6+}$ (W^{6+}) charge transfer (CT) transitions. First peak is usually observed in compounds, which contain isolated tetrahedral coordinated MoO_4 or WO_4 species [38, 40]. The second peak most likely refers to polymolybdate-like structure containing octahedral coordinated Mo ions (MoO_6 species) [36], while the third signal probably related to polytungstates or WO_3 cluster contained octahedral coordinated W ions (WO_6 species) [38]. The intensity of the band from isolated tetrahedral coordinated molybdate (tungstate) ions is much higher than from polymolydates (polytungstates).

Besides α-$NiMoO_4$ phase, the precursor calcined at 500 °C contains WO_3 (PDF#00-033-1387, $a = b = 7.298$, $c = 3.899$ Å) with the CSR size $D \sim 8$ nm, $NiWO_4$ (PDF#00-015-0755, $a = 4.912$, $b = 4.60$, $c = 5.665$ Å) with CSR size $D = 19$ nm, and NiO (PDF#00-047-1049, $a = b = c = 4.177$ Å), $D \sim 10$ nm.

The Raman spectra of the NiMoW-500 sample is characterized by the set of bands at 540, 690, 760, 853 cm^{-1} with the shoulders at 815, 880 and 920 cm^{-1}, as well as 962 and 990 cm^{-1}. Signals at 990 cm^{-1} with the 815 cm^{-1} belong to the modes from MoO_3. The peaks at 962, 920 and $\sim$ 700 cm^{-1} characterize nickel molybdate, and the bands at 880 and 690 cm^{-1} correspond to nickel tungstate. On the other hand, the band in the range of 715 cm^{-1} accompanied by the band at around 805 cm^{-1} can be attributed to the W–O–W deformation mode, W–O bending modes and a W–O stretching vibration characteristic of octahedral WO_3-like species (or crystalline WO_3) and may overlap with the signals of the above compounds [38]. The modes from carbon compounds completely disappear.

The UV-Vis DR spectrum of the NiMoW-500 precursor contains the new bands at 740 and 820 nm which are likely associated with Ni^{2+} ions octahedral coordinated to molybdate ions in nickel molybdate [41,42]. The last band is coming from the distortion of octahedral Ni^{2+} by incorporation to MoO_4^{2-}. Nickel ions in the $NiWO_4$ structure can also absorb in this area too [43].

3.1.3. Intermediate conclusions. Summarizing effects seen in the precursor samples, the following scheme can be provided (Fig. 5). First, the precursor obtained after spray drying contains molybdenum, tungsten and nickel citrate complexes. When heat treatment temperature increases to 300 °C, citrates decompose and form variations of acotonic and itaconic compounds followed by the formation of carbon-containing compounds, like coke. Then, the heating to more than 450 °C results in the removal of carbon and other products of citrate's decomposition and formation of crystal phases – both individual Ni, Mo or W oxides and mixed oxides.

FIG. 5. Scheme on the possible reactions being occurred in the NiMoW precursor

3.2. Structure of NiMoW catalysts

Before describing and discussing the structural data on the bulk NiMoW catalyst, it should be emphasized that all structural changes of the NiMoW precursor are not significantly affected by calcination of catalysts granules, because final calcination temperature is equal or less than calcination of the NiMoW precursor.

According to CHNS analysis (Table 1), residuals of citric acid decomposition products present in the catalysts even at high temperatures. Carbon content decreases from 7 to 0.8 wt.%, when calcination temperature increases from 300 to 500 °C. It is noted that carbon content is high in the NiMoW-300-300 and NiMoW-450-300 catalysts. Then, we can suggest that decomposition of citric acid is complicated in bulk catalysts comparing to supported samples [35, 44, 45]

possibly due to its hiding in the catalyst volume. Moreover, X-ray amorphous properties seen for the NiMoW precursor calcined at 300 °C could be caused by even distribution of atoms of active metals in the presence of high amount of carbon in the samples [46].

TABLE 1. CHNS analysis data of catalysts

Sample	C% wt.	H% wt.	N% wt.	S% wt.
NiMoW-300-300	7.4	1.4	1.4	0
NiMoW-450-300	3.2	0.7	0.7	0
NiMoW-500-300	0.8	0.6	0	0

Another point is the presence of nitrogen in granulated catalysts. Obviously, nitrogen is caused by the use of nitric acid during plasticization and can be also present as a residual nitrogen in pseudoboehmite (specified by the synthesis procedure). Then, the increase in calcination temperature of granules results in the decrease of nitrogen content. Some of nitrogen could be present from ammonium heptamolybdate used in the synthesis. It explains the difference between the NiMoW-300-300 and NiMoW-450-300 samples. It is not obvious, how nitrogen will influence catalysts activity. Possibly, similar effects of HDS activity worsening can be pointed out [47].

The features of the precursor transformation during its calcination are confirmed by data of thermal analysis (Fig. 6). DTG curves demonstrate three-stages weight loss. The first stage at 80 – 100 °C is caused by desorption of physically adsorbed water. The second one at 430 – 445 °C is due to phase transformation of pseudoboehmite to γ-Al_2O_3 [21,48] or to decomposition of various citrates to oxides. The main difference between the samples is observed in DTG/DSC curves. The NiMoW-300-300 and NiMoW-450-300 catalysts demonstrate strong endo-effect at 554 and 578 °C, respectively, due to the formation of stable nickel molybdates and tungstates ($NiMoO_4$ and $NiWO_4$) [29,31]. The TG/DTG/DSC curves of the NiMoW-500-300 catalyst in this temperature region are plateau.

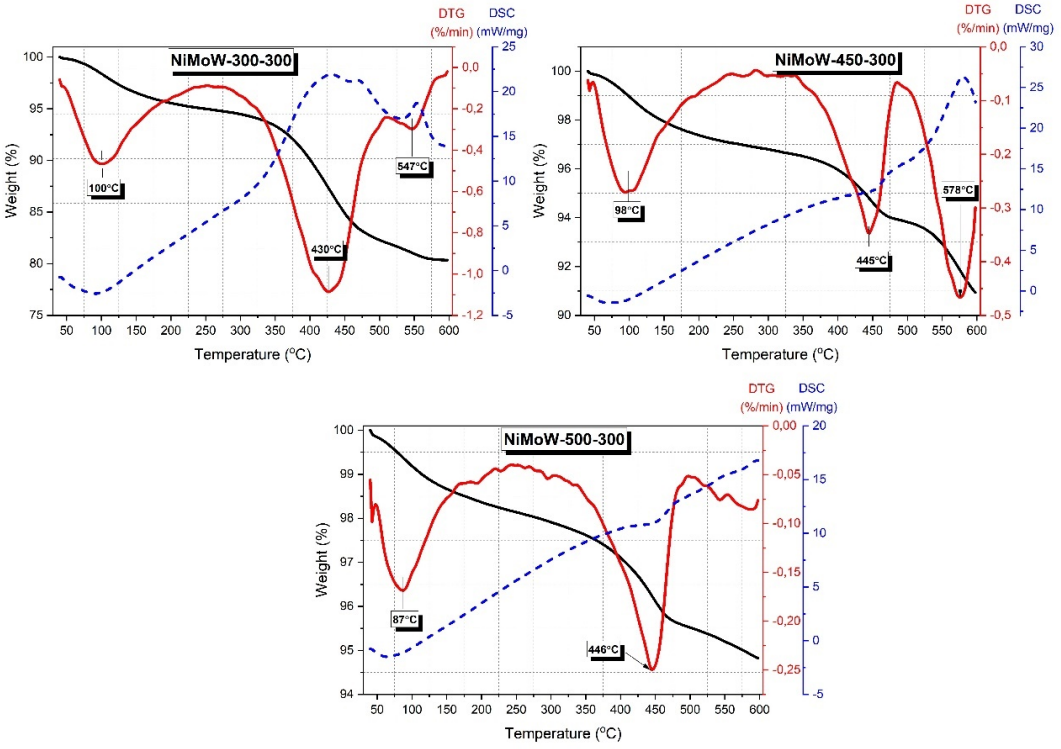

FIG. 6. TG and DTG curves of NiMoW-300-300, NiMoW-450-300, NiMoW-500-300, catalysts

Using IR, UV-Vis DR and Raman spectroscopy, the structural properties of the NiMoW granulated catalyst samples in the oxide form were compared. The UV-Vis DR spectrum of the NiMoW-300-300 catalysts (Fig. 4B) shows a decrease in signals associated with the carbon material compared to the spectrum of the NiMoW-300 precursor (Fig. 4A). The appearance of three strong broad bands centered at 220, 290 and 330 nm could be assigned to $O^{2-} \rightarrow Mo^{6+}$ (W^{6+}) CT transitions. Apparently, some of the polyoxometalate anions react with Al–OH groups of pseudoboehmite to form probably $(Al_s)_2Mo(W)O_4$ surface species. This promotes the release of polymolybdate (polytungstate anions) from the organic

matrix. Most of the Ni^{2+} ions remain uniformly distributed and shielded by the organic amorphous matrix. Calcination of the NiMoW precursor at higher temperatures leads to the disappearance of the signal from the carbon material in the spectra of the NiMoW-450-300 and NiMoW-500-300 catalysts. The spectra of the NiMoW-450-300 and NiMoW-500-300 catalysts demonstrate more intense signals in the region of $O^{2-} \rightarrow Mo^{6+}$ (W^{6+}) CT transitions compared with the corresponding precursors. This may be the result of the anchoring of polymolybdate and polytungstate structures on the Al–OH groups of pseudoboehmite. The state of Ni^{2+} ions in NiMoW-450-300 and NiMoW-500-300 catalysts differs slightly from corresponded precursors. In all compounds, Ni^{2+} ions are stabilized in octahedral coordination. Additionally, there is an increase in intensity in the long-wavelength region of the spectrum of the NiMoW-450-300 sample, which may indicate Ni^{2+} ions in the structure of molybdate or tungstate.

The IR spectra of the NiMoW catalysts are shown in Fig. 7. Three intense bands at 480, 630 and 740 cm^{-1} in the framework vibration range as well as four peaks at 1070, 1160 and 3090, 3303 cm^{-1} characterize a well crystallized boehmite [49]. Moreover, the spectra of all samples demonstrate a weak signal at 1384 cm^{-1} related to residual NO_3- ions. The bands at 1715 (νC=O in $-$COOH) and 2855, 2925, 2960 cm^{-1} (ν ($-CH_2-$, $-CH_3$)) in the spectrum of the NiMoW-300-300 sample are assigned to residual citric acid fragments, while the bands at 1590 (ν_{as} COO$-$) and 1410 cm^{-1} (ν_s COO$-$) are attributed to carboxylate groups that were binding with the aluminum atoms of the boehmite surface [50]. The bands at about 1590 – 1300 cm^{-1} in the spectrum of the NiMoW-450-300 sample relate to carbonate-carboxylate compounds, but the only peak at 1630 cm^{-1} in this region for the NiMoW-500-300 sample is due to adsorbed water. The intensity of the boehmite signals for the NiMoW-500-300 catalyst is the highest, while it is slightly higher for the NiMoW-450-300 then for the NiMoW-300-300 catalyst. Thus, higher calcination temperature of the NiMoW precursor decreases the residual content of carbon-containing fragments (it is also shown in Table 1). It complicates the transformation of pseudoboehmite structure to alumina. To confirm that, we made additional studies of the samples by XRD method (Fig. A1, Appendix).There was no alumina phase in the samples, which granules were calcined at 300 °C. But when calcination temperature of the granules becomes 400 °C, alumina phase is observed from high-intensive peaks in XRD curves. Possibly, the samples calcined at 300 °C also contain some γ-Al_2O_3, but its amount is very small, and reflections are overlapped by other phases. Another point is that boehmite starts to transform at higher temperatures as it seen from IR spectroscopy.

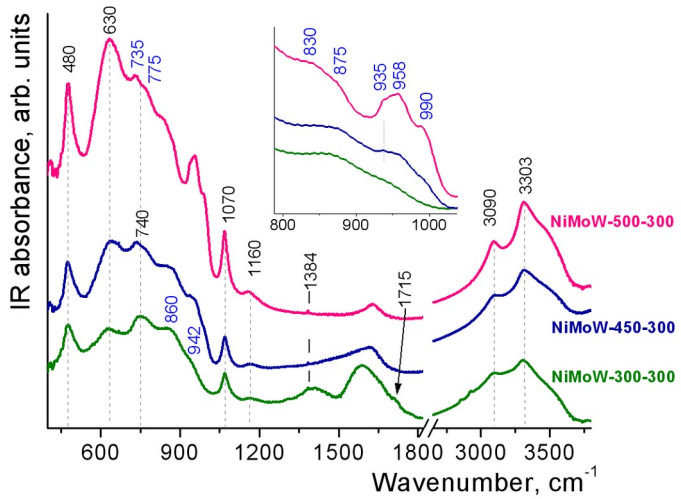

FIG. 7. IR spectra of NiMoW-X-300 (where $X = 300$, 450 and 500 °C) catalysts. The inset shows enlarged fragment of spectra

Two bands at 942 and 860 cm^{-1} in the spectrum of the NiMoW-300-300 sample could be attributed to the vibrations of the distorted MoO_6 units in polymolybdate anions. The band at 958 with the shoulder at 935 cm^{-1} in the spectra of the NiMoW-450-300 and NiMoW-500-300 samples characterize a bulk α-$NiMoO_4$ [51, 52]. A group of signals at about 990 and 875 cm^{-1} is assigned to bulk MoO_3 [53]. The intensity of the signals associated with nickel molybdate and molybdenum oxide is higher for the NiMoW-500-300 catalyst than for the NiMoW-300-300 catalyst. Therefore, the higher calcination temperature of the NiMoW precursor leads to higher crystallization degree of nickel molybdate and molybdenum oxide that is confirmed by UV-Vis DRS. In addition, the well resolved peaks at 830, 775 and 735 cm^{-1} are observed in the spectrum of the NiMoW-500-300 sample. The first band is attributed to a bulk $NiWO_4$ [43, 54], while the second and the third peaks may be associated with the formation of WO_3 [38, 55]. The signal of Ni–O bonds in NiO overlaps with the intense absorbance of pseudoboehmite and cannot be detected by the used method.

The Raman spectra of the catalysts confirm the observed results (Fig. 3B). The background significantly grows for all catalysts that is probably caused by the presence of OH groups in the alumina binder. The addition of the binding agent leads to the decrease in the intensity of the signals from carbon in both catalysts calcined at 300 and 450 °C. Moreover, the

signals in the spectrum of the NiMoW-450-300 from Mo and W oxides also decrease and almost disappear. The spectrum of the NiMoW-500-300 is similar to the precursor one. The spectra also contain the band at 1786 cm^{-1}, which is related to vibrations of the keto group >C=O in aliphatic or aromatic esters, products of the decomposition of citric acid.

The granulated bulk catalysts were studied by nitrogen adsorption-desorption method. Specific surface area (SSA) and pore volume (V_p) significantly decrease from 122 to 61 m^2/g with the increase of calcination temperature of the precursor from 300 to 450 °C (Table 2). It can be caused by decomposition and removal of citrate in complexes, transformation of Ni, Mo and W compounds and possible sintering of formed oxides. The SSA and especially V_p values increase from 61 to 83 m^2/g and from 0.12 to 0.17 cm^3/g when calcination temperature of the precursor was increased to 500 °C (Table 2). The average pore diameter (D_p) shifts slightly toward higher values from 5.2 to 8.4 nm with increasing precursor calcination temperature from 300 to 450 – 500 °C.

TABLE 2. Textural properties of the calcined catalysts

Sample	SSA, m^2/g	V_p, cm^3/g	D_p, nm
NiMoW-300-300	122	0.16	5.2
NiMoW-450-300	61	0.12	7.7
NiMoW-500-300	83	0.17	8.4

Formation of bulk systems requires consideration of porous structure for the transportation of feedstock molecules. Shape of pores in bulk catalysts can be defined from adsorption-desorption isotherms (Fig. A2, Appendix). According to classification [22], the form of isotherms is similar to IV(a) type specific for mesoporous materials. Hysteresis loops of isotherms indicate capillary condensation of nitrogen in mesopores. All studied catalysts have similar hysteresis loops classified to H3 type, which is characteristic for materials consisting of non-rigid particle aggregates of irregular size and/or shape. On other point of view, this type of hysteresis loop can be observed for macroporous structures, which are not filled by condensate. Since nitrogen adsorption-desorption method cannot measure macropores, we can assume that the lack of the developed mesoporous structure (especially small mesoporous volume) is compensated by transportation pores. This assumption was confirmed by the results of mercury porosimetry (Fig. 8). The increase in the volume of macropores occurred when the calcination temperature of the precursor was increased.

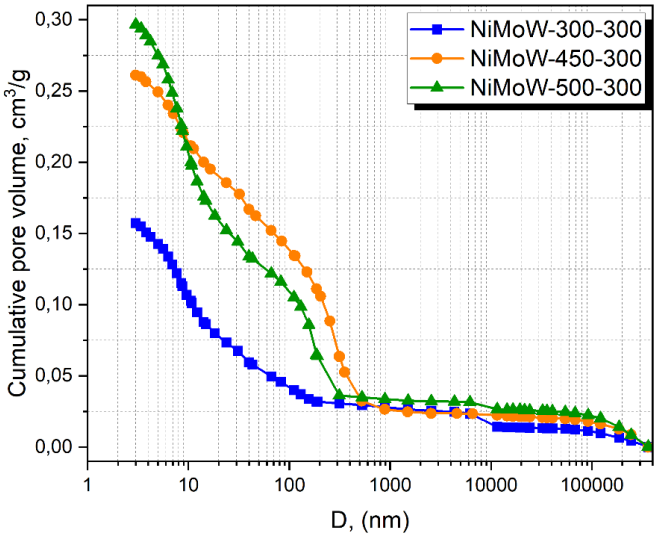

FIG. 8. Dependences of the volume of cumulative on the pore diameter ($\log D$) obtained from the results of mercury intrusion for calcined catalysts

The changes in mesoporosity are better seen from the pore size distribution from nitrogen adsorption-desorption (Fig. A2, Appendix). The NiMo-300-300 catalyst has wide pore size distribution with a strong maximum at 4 nm and smooth curve in the range of 5 – 15 nm. Calcination at 450 – 500 °C resulted in the formation of bimodal pore size distribution curves with the first maxima at 4 nm and the second maxima at 5 – 15 nm. Comparing three catalysts we can conclude that calcination led to the formation of mesopores of 5 – 15 nm.

3.3. Effect of calcination temperature on catalysts activity in HDT of real feedstocks and structure of sulfide catalysts

The data of hydrotreating of SRVGO at 340 – 360 °C are given in Table 3. The catalysts show worsening in HDS activity with the increase in the calcination temperature from 300 to 500 °C. HDN activity also becomes worse. This tendency is actual for all process temperature range. Therefore, the best choice of temperature regimes is 300 °C. It should be noted that the comparison of the bulk catalyst prepared in a similar way as NiMoW-300-300 catalyst with the supported catalyst was carried out earlier [56]. It was shown that the bulk catalyst was superior in activity to the supported one. Then, we can suppose that the activity of the NiMoW-300-300 catalyst in SRVGO hydrotreatment will be also higher.

TABLE 3. Results of catalytic tests in hydrotreating of SRVGO

Temperature, °C / Sample	340		350		360	
	S, ppm	N, ppm	S, ppm	N, ppm	S, ppm	N, ppm
NiMoW-300-300	1461	800	1061	711	775	597
NiMoW-450-300	2112	913	1596	835	1157	738
NiMoW-500-300	2345	937	1812	854	1406	796

The catalysts in the sulfide state were washed in toluene after testing and investigated by low-temperature nitrogen adsorption-desorption method (Table 4). Values of SSA and V_p decreased compared to the calcined catalysts. The observed result is related to the transition of active metals into sulfide form and to the acceleration of carbon during testing. The formation of active metal sulfides in the catalysts is described below in the description of the XPS results. However, the difference between the samples in SSA and V_p values became insignificant considering the method error of 5 %. The exception is the NiMoW-500-300 sample. The pore volume (0.10 cm^3/g) for the mentioned sample is higher than that of the other samples (Table 4). The trends in the change of pore size distribution with increasing precursor calcination temperature after the reaction are maintained (Fig. A3, Appendix). The NiMoW-500-300 sample contains large number of pores with the diameters of 5 – 15 nm compared to the others. Thus, in terms of textural characteristics, it is the most preferable catalyst. However, this catalyst has the lowest activity in HDS and HDN reactions (Table 3). Then, the changes in the catalytic activity are related to the properties of the active metals.

TABLE 4. Textural properties of the sulfided catalysts

Sample	SSA, m^2/g	V_p, cm^3/g	D_p, nm
NiMoW-300-300	35	0.07	8.4
NiMoW-450-300	22	0.06	11.0
NiMoW-500-300	43	0.10	9.6

Sulfide catalysts before testing were studied by HRTEM and SEM methods. Fig. 9 shows HRTEM images of the studied catalysts. It is seen that there are slabs of active component particles which are localized over alumina as well as bulk particles. The transition of active metals to alumina binder can occur at the granulation stage. On the one hand, this phenomenon can be an advantage for catalysts activity due to the formation of more dispersed active phase, which is similar in structure to the high active "Ni–Mo–S" phase. On the other hand, there can be the decrease of "bulk active sites" concentration that could decrease catalysts activity. However, it is a question for the future discussion.

The increase in the calcination temperature of the precursor powder used for granulation results in the increase of the length of active component particles and their stacking. In addition, there is a visual enlargement of bulk particles in catalysts.

Metals distribution in catalysts given in Figs. 10 and A4–5 (Appendix) demonstrates separately allocated nickel particles that is likely caused by the extraction of nickel from the volume to the surface during sulfidation procedure. The images of the NiMoW-300-300 (Fig. 10) catalyst also show that sulfur and nickel have similar distribution areas that can indicate the formation of nickel sulfides. Similar areas of sulfur and tungsten accumulations are pointed out, while molybdenum distribution is uniform.

The images of the NiMoW-450-300 (Fig. A4, Appendix) and NiMoW-500-300 (Fig. A5, Appendix) catalysts additionally contain areas, where Mo and W are concentrated in the inner part, while Ni is in the outside part forming rim (Fig. 11). The increase in calcination temperature leads to the pronunciation of the effect. It is seen that the higher calcination temperature, the greater encapsulation of Mo and W by Ni. At the same time, sulfur is distributed evenly over all areas of localization of three metals.

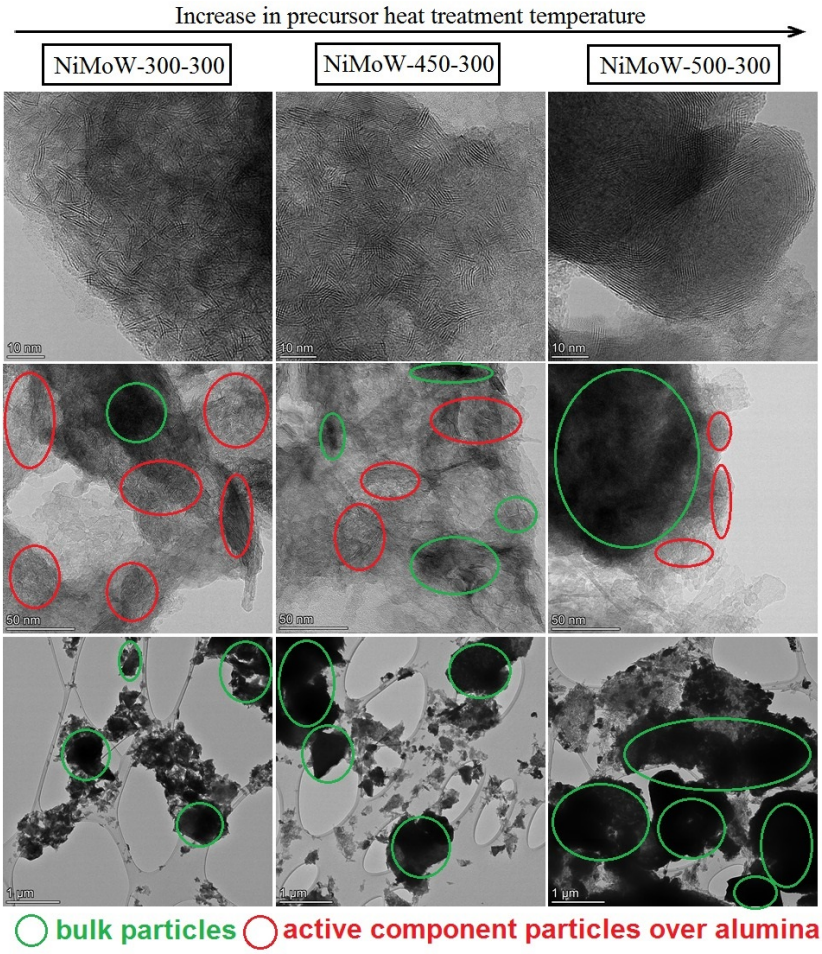

FIG. 9. HRTEM images of the NiMoW-300-300, NiMoW-450-300 and NiMoW-500-300 catalysts before testing

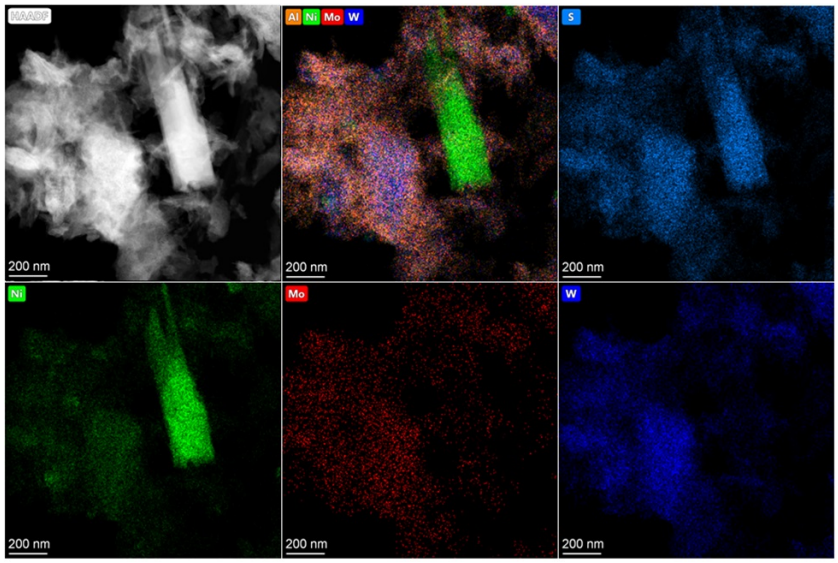

FIG. 10. HAADF data on the NiMoW-300-300 catalyst before testing

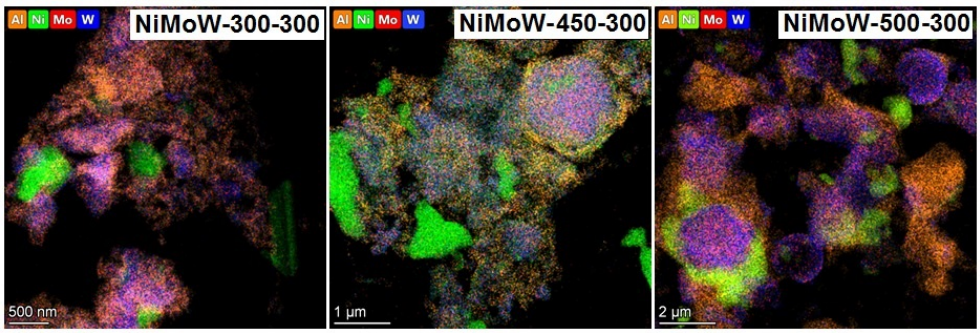

FIG. 11. HAADF data on the catalysts after testing to demonstrate encapsulation of metals

The NiMoW-300-300 and NiMoW-500-300 catalysts were studied by XPS to obtain additional information on the state of active metals. Fig. 12A demonstrates Mo3d spectra for the studied samples. The catalysts have different surface concentration of molybdenum. The surface concentration of Mo in the NiMoW-300-300 catalyst is 2.6 %, and in the NiMoW-500-300 catalyst – 0.9 % (Table 5). All detected Mo on the catalysts surface is in the Mo^{4+} state in both catalysts, because Mo3d spectrum contains only one doublet with the binding energy of $Mo3d_{5/2} \sim 228.9$ eV [57, 58]. There are no peaks with E_b close to 230.7 and ~ 232.6 eV corresponding to Mo^{5+} and Mo^{6+}, respectively. The peaks at ~ 226.3 and ~ 233.4 eV in all samples relate to sulfur (region S2s) and are characterized for sulfur in sulfides (S^{2-} and S_2^{2-}) and sulfates (S^{6+}), respectively.

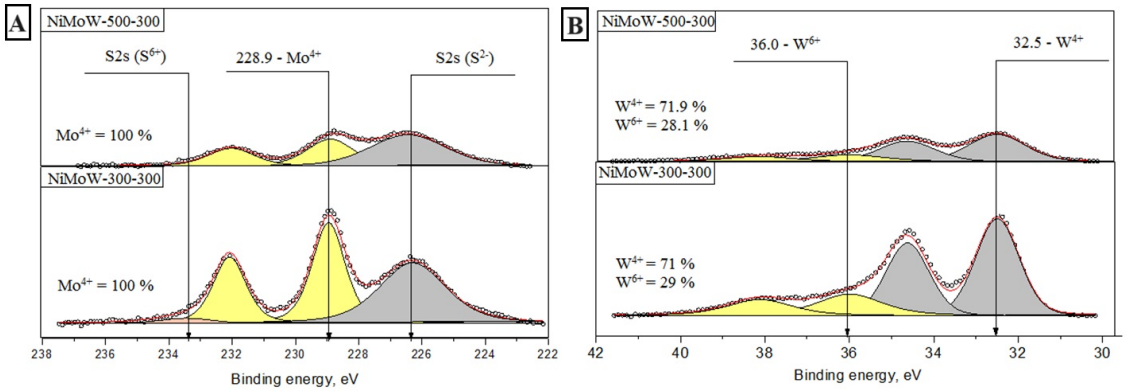

FIG. 12. Mo3d (A) and W4f (B) XPS spectra of the NiMoW-300-300 and NiMoW-500-300 catalysts after testing

TABLE 5. XPS data of studied catalysts

Parameter	NiMoW-300-300	NiMoW-500-300
Al – %	19.4	17.7
S – %	21.7	11.1
Mo – %	2.6	0.9
W – %	2.9	1.0
Ni – %	3.6	1.7
Mo/S	0.12	0.08
Ni/S	0.16	0.16
W/Mo	1.13	1.14

The surface concentration of tungsten is also lower in NiMoW-500-300 catalyst (1 %) than in NiMoW-300-300 (2.9 %) (Table 5, Fig. 12B). It can be caused by capsulation of tungsten during calcination of the precursor. W4f spectra of studied catalysts are decomposed by two doublets with binding energies $W4f_{7/2} \sim 32.5$ and 36.0 eV, respectively

(Fig. 12B). The peak with the binding energy ~ 32.5 eV can be assigned to tungsten in the W^{4+} state that is caused by the transition of WO_3 to WS_2 during sulfidation [59]. The fraction of W^{4+} from detected surface tungsten is 71.9 % in the NiMoW-300-300 catalyst and 71.0 % in the NiMoW-500-300 catalyst. The rest of tungsten is in the W^{6+} state (i.e. tunsten oxide) and is confirmed by the peak at ~ 36.0 eV [13, 60].

The intensity of the Ni2p spectra was 2.1 times higher in the NiMoW-300-300 sample compared to NiMoW-500-300 (Fig. 13A). The $Ni2p_{3/2}$ spectra of both catalysts contain two peaks with the binding energies ~ 854.0 and ~ 856.2 eV. The peak at ~ 854.0 eV relates to the Ni^{2+} in NiMoS phase [61] and/or to trimetallic NiMoWS phase [13]. The fraction of nickel in these phases is more than 80 % in both catalysts. However, the amount of NiMoS phase in NiMoW-300-300 catalyst is much higher considering the surface concentration of nickel. The peak at 856.2 eV is specific for the Ni^{2+} in NiO that is confirmed by the presence of intensive satellite at $\sim 861 - 862$ eV [61].

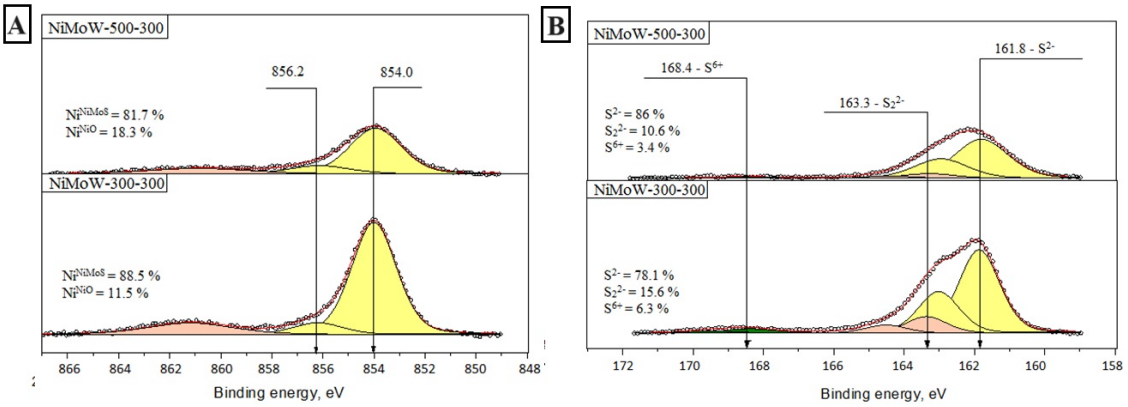

FIG. 13. Ni2p (A) and S2p (B) XPS spectra of the NiMoW-300-300 and NiMoW-500-300 catalysts after testing

The S2p XPS spectra of studied samples contain the $S2p_{3/2}$ peak with the binding energy at 168.4 eV (Fig. 13B). The surface sulfur concentration is also significantly higher in the NiMoW-300-300 catalyst than in the NiMoW-500-300 sample (Table 5). It is the feature of the S^{6+} in sulfates SO_4^{2-} [62]. In the range of lower binding energy values there are two doublets with the binding energy at 161.8 and ~ 163.3 eV. They are characteristic for sulfides like S^{2-} and S_2^{2-}, respectively [62–64]. The ratio of S^{2-} to S_2^{2-} increases with calcination temperature of the precursor as well as there is the decrease in sulfate sulfur.

Summarizing the XPS data it was noted that an increase in the precursor calcination temperature from 300 to 500 leads to a decrease in the number of surface atoms of active metals. The NiMoW-300-300 catalyst is the best in the content of the most active form of Ni, Mo and W. The higher calcination temperature results in the formation of more oxide forms of active metals possibly due to the removal of citric acid residuals. Moreover, there is the decrease in the ratio of active metals to the binding component – alumina, which could indirectly indicate the aggregation of active metals.

4. Conclusion

The present work studies the effect of calcination temperature of the precursor on physico-chemical properties of bulk NiMoW catalysts. According to thermal analysis and plasticizing properties of the NiMoW precursor, three calcination temperatures were chosen – 300, 450 and 500 °C.

It is found that calcination of the precursor at 300 °C results in the formation of X-ray amorphous NiMoW precursor that is likely caused by incomplete decomposition of citric acid and its transformation into amorphous carbon. XRD patterns of the catalysts with calcination temperature 450 and 500 °C demonstrate reflexes from nickel molybdate, individual nickel and tungsten oxides and nickel tungstate. These data are also confirmed by UV-Vis spectra, which show the increase of crystallization degree of nickel molybdate and molybdenum oxide as well as the decrease of the amount of carbon containing compounds. It makes it difficult to convert pseudoboehmite into alumina.

The influence of calcination temperature of the precursor on textural properties of the related bulk catalysts is not obvious. When temperature is 300 or 450 °C, there is the decrease in the specific surface area and pore volume of the catalysts that is likely caused by decomposition of citric acid and other transformations of the precursor compounds formed during plasticizing with nitric acid and by possible sintering of the obtained oxides. On the contrary, the increase in precursor's calcination temperature to 500 °C results in the increase in textural characteristics of granulated catalyst due to its re-structurization. Despite the improved textural properties, the bulk catalyst prepared from the Ni–Mo–W precursor calcined at 500 °C did not demonstrate high activity in hydrotreating of SRVGO. The most active catalyst in hydrotreatment of SRVGO was the one prepared from the precursor calcined at 300 °C.

Investigation of the sulfide catalysts showed that after granulation of the catalysts some part of active metals reacted with the alumina binding agent and formed "Ni–Mo–S"-like particles. The other part was presented in the form of various bulk species, individual or mixed. The increase in calcination temperature from 300 to 500 °C resulted in the increase in the formation of more amount of bulk nickel sulfides and capsulation of Mo and W which were rounded by nickel atoms. According to the XPS analysis data, it led to the decrease in the number of active metals in their most active sulfide forms. The catalysts with higher calcination temperature of the precursor or granules contain more active metals in the oxide form.

Appendix

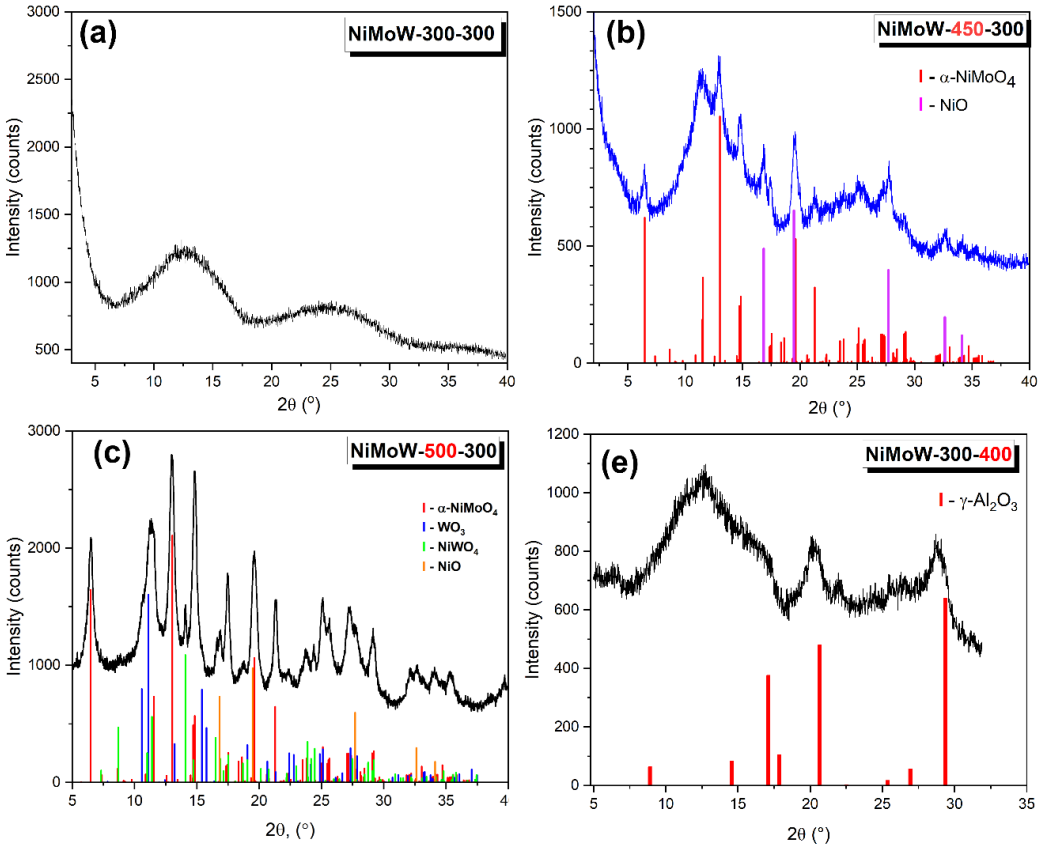

FIG. A1. XRD data of granulated catalyst with different precursor calcination temperature and catalysts calcination temperature

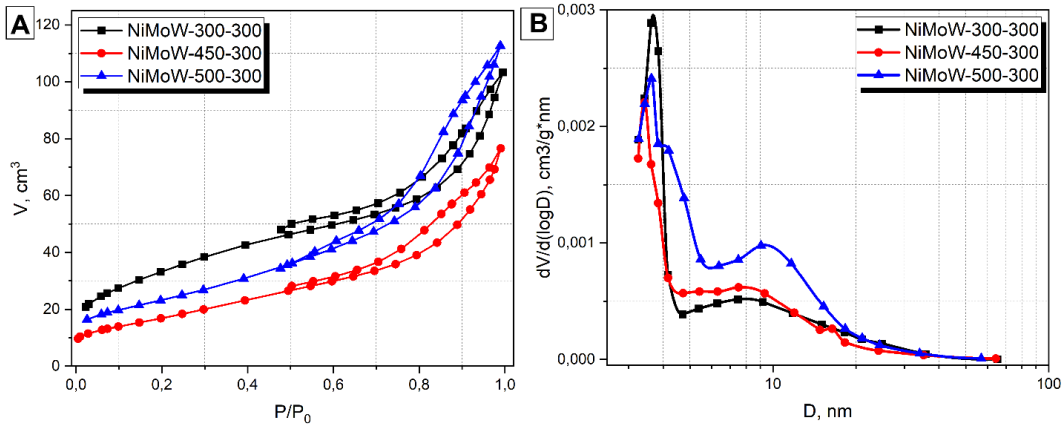

FIG. A2. Nitrogen adsorption-desorption isotherms and pore size distribution curves for granulated calcined catalysts

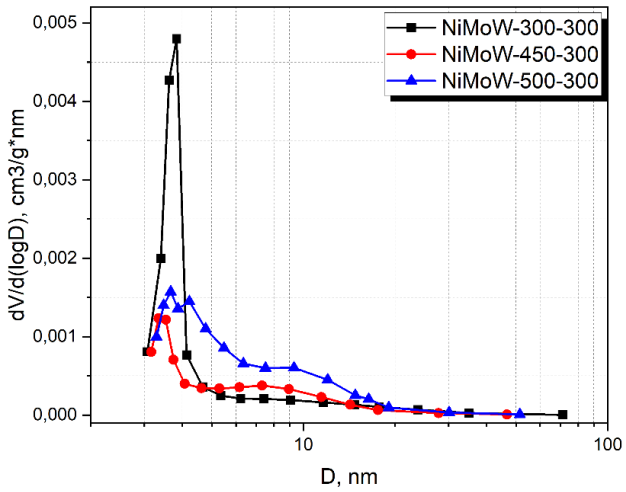

FIG. A3. Pore size distribution curves for sulfided catalysts after reaction

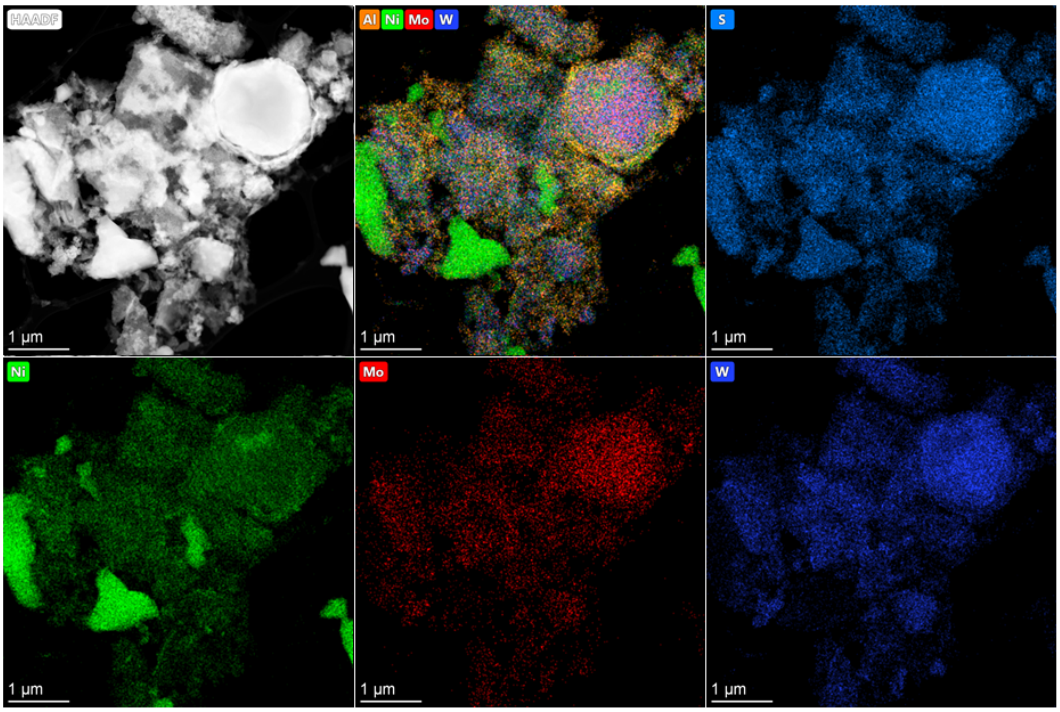

FIG. A4. HAADF data on the NiMoW-450-300 catalyst before testing

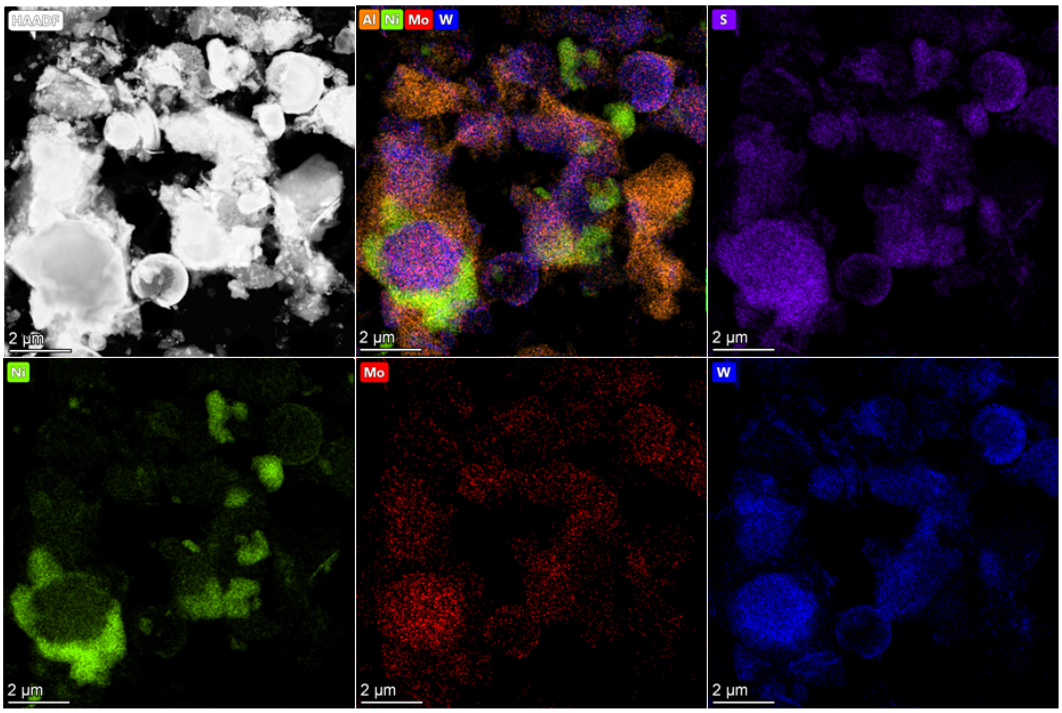

FIG. A5. HAADF data on the NiMoW-500-300 catalyst before testing

References

[1] Tanimu A., Alhooshani K. Advanced Hydrodesulfurization Catalysts: A Review of Design and Synthesis. *Energy and Fuels*, 2019, **33**, P. 2810–2838.

[2] Díaz de León J.N., Ramesh Kumar C., Antúnez-García J., Fuentes-Moyado S. Recent Insights in Transition Metal Sulfide Hydrodesulfurization Catalysts for the Production of Ultra Low Sulfur Diesel: A Short Review. *Catalysts*, 2019, **9**, 87.

[3] Topsøe H., Clausen B.S., Candia R., Wivel C., Mørup S. In situ Mössbauer emission spectroscopy studies of unsupported and supported sulfided Co-Mo hydrodesulfurization catalysts: Evidence for and nature of a Co–Mo–S phase. *J. Catal.*, 1981, **68**, P. 433–452.

[4] Lauritsen J.V., Kibsgaard J., Olesen G.H., Moses P.G., Hinnemann B., Helveg S., Nørskov J.K., Clausen B.S., Topsøe H., Lægsgaard E., Besenbacher F. Location and coordination of promoter atoms in Co- and Ni-promoted MoS_2-based hydrotreating catalysts. *J. Catal.*, 2007, **249**, P. 220–233.

[5] Plantenga F.L., Cerfontain R., Eijsbouts S., Houtert F., Anderson G.H., Miseo S., Soled S., Riley K., Fujita K., Inoue Y. "NEBULA": A hydroprocessing catalyst with breakthrough activity. *Stud. Surf. Sci. Catal.*, 2003, **145**, P. 407–410.

[6] Eijsbouts S., Plantenga F., Leliveld B., Inoue Y., Fujita K. STARS and NEBULA – New Generations of Hydroprocessing Catalysts for the Production of Ultra Low Sulfur Diesel. *Prepr. Symp. – Am. Chem. Soc., Div. Fuel Chem.*, 2003, **48**, P. 494–495.

[7] Thomazeau C., Geantet C., Lacroix M., Danot M., Harlé V., Raybaud P. Predictive approach for the design of improved HDT catalysts: γ-Alumina supported (Ni, Co) promoted $Mo_{1-x}W_xS_2$ active phases. *Appl. Catal. A Gen.*, 2007, **322**, P. 92–97.

[8] Cervantes-Gaxiola M.E., Arroyo-Albiter M., Pérez-Larios A., Balbuena P.B., Espino-Valencia J. Experimental and theoretical study of NiMoW, NiMo, and NiW sulfide catalysts supported on an AlTiMg mixed oxide during the hydrodesulfurization of dibenzothiophene. *Fuel*, 2013, 113, P. 733–743.

[9] Krebs E., Silvi B., Daudin A., Raybaud P. A DFT study of the origin of the HDS/HydO selectivity on Co(Ni)MoS active phases. *J. Catal.*, 2008, **260**, P. 276–287.

[10] Shan S., Liu H., Yue Y., Shi G., Bao X. Trimetallic WMoNi diesel ultra-deep hydrodesulfurization catalysts with enhanced synergism prepared from inorganic–organic hybrid nanocrystals. *J. Catal.*, 2016, **344**, P. 325–333.

[11] Varakin A.N., Mozhaev A.V., Pimerzin A.A., Nikulshin P.A. Comparable investigation of unsupported MoS_2 hydrodesulfurization catalysts prepared by different techniques: Advantages of support leaching method. *Appl. Catal. B Environ.*, 2018, **238**, P. 498–508.

[12] Yin C., Dong C., Kong Y., Li K., Zhang H., Liu D., Liu C. Effects of Aging Treatment on the Hydrotreating Performance of the Unsupported Catalyst. *Ind. & Eng. Chem. Res.*, 2019, **58**, P. 2683–2688.

[13] Nadeina K.A., Budukva S.V., Vatutina Y.V., Mukhacheva P.P., Gerasimov E.Y., Pakharukova V.P., Prosvirin I.P., Larina T.V., Klimov O.V., Noskov A.S., Atuchin V.V. Optimal Choice of the Preparation Procedure and Precursor Composition for a Bulk Ni–Mo–W Catalyst. *Inorganics*, 2023, **11**, 89.

[14] Mukhacheva P.P., Vatutina Y.V., Nadeina K.A., Budukva S.V., Pakharukova V.P., Danilova I.G., Panafidin M.A., Klimov O.V., Noskov A.S. Effects of Heat Treatment Temperature on the Physicochemical Properties and Catalytic Performance of Bulk Ni–Mo–W Catalysts. *Pet. Chem.*, 2023, **63**, P. 1302–1310.

[15] Wang L., Zhang Y., Zhang Y., Jiang Z., Li C. Ultra-Deep Hydrodesulfurization of Diesel Fuels on Trimetallic NiMoW Sulfide Catalysts. *Chem. – A Eur. J.*, 2009, **15**, P. 12571–12575.

[16] Chowdari R.K., Díaz de León J.N., Fuentes-Moyado S. Effect of sulfidation conditions on the unsupported flower-like bimetallic oxide microspheres for the hydrodesulfurization of dibenzothiophene. *Catal. Today*, 2022, **394–396**, P. 13–24.

[17] Ouyang X., Kuperman A. Multi-metallic bulk hydroprocessing catalysts, Patent 2022269376, 2021.

[18] Liu H., Yin C., Liu B., Li X., Li Y., Chai Y., Liu C. Effect of Calcination Temperature of Unsupported NiMo Catalysts on the Hydrodesulfurization of Dibenzothiophene. *Energy & Fuels*, 2014, **28**, P. 2429–2436.
[19] Yang C., Hu A., Dai Q., Yang Q., Hou R., Liu Z. Study on the Performance of Ni–MoS_2 Catalysts with Different MoS_2 Structures for Dibenzothiophene Hydrodesulfurization. *ACS Omega*, 2023, **8**, P. 41182–41193.
[20] Nadeina K.A., Budukva S.V., Vatutina Y.V., Mukhacheva P.P., Gerasimov E.Y., Pakharukova V.P., Klimov O.V., NoskovA.S. Unsupported Ni–Mo–W Hydrotreating Catalyst: Influence of the Atomic Ratio of Active Metals on the HDS and HDN Activity. *Catalysts*, 2022, **12**, 1671.
[21] Danilevich V.V., Nadeina K.A., Gerasimov E.Y., Shefer K.I., Klimov O.V., Noskov A.S. Synthesis and characterization of lanthanum-modified pseudoboehmite – The precursor of alumina supports and catalysts. *Microporous Mesoporous Mater.*, 2022, **335**, 111800.
[22] Thommes M., Kaneko K., Neimark A.V., Olivier J.P., Rodriguez-Reinoso F., Rouquerol J., Sing K.S.W. Physisorption of gases, with special reference to the evaluation of surface area and pore size distribution (IUPAC Technical Report). *Pure Appl. Chem.*, 2015, **87**, P. 1051–1069.
[23] Moulder J.F. *Handbook of X-ray Photoelectron Spectroscopy*, Physical Electronics Division, Perkin-Elmer Corporation, 1992.
[24] Scofield J.H. Hartree-Slater subshell photoionization cross-sections at 1254 and 1487 eV. *J. Electron Spectros. Relat. Phenomena*, 1976, **8**, P. 129–137.
[25] Gajbhiye N.S., Balaji G. Synthesis, reactivity, and cations inversion studies of nanocrystalline $MnFe_2O_4$ particles. *Thermochim. Acta*, 2002, **385**, P. 143–151.
[26] Bocher L., Aguirre M.H., Robert R., Trottmann M., Logvinovich D., Hug P., Weidenkaff A. Chimie douce synthesis and thermochemical characterization of mesoporous perovskite-type titanate phases. *Thermochim. Acta*, 2007, **457**, P. 11–19.
[27] Rajendran M., Rao M.S. Formation of $BaTiO_3$ from Citrate Precursor. *J. Solid State Chem.*,1994, **113**, P. 239–247.
[28] Rajendran M., Rao S.M. Synthesis and characterization of barium bis(citrato) oxozirconate(IV) tetrahydrate: A new molecular precursor for fine particle $BaZrO_3$. *J. Mater. Res.*, 1994, **9**, P. 2277–2284.
[29] Kovács T.N., Hunyadi D., de Lucena A.L.A., Szilágyi I.M. Thermal decomposition of ammonium molybdates. *J. Therm. Anal. Calorim.*, 2016, **124**, P. 1013–1021.
[30] Fait M.J.G., Lunk H.-J., Feist M., Schneider M., Dann J.N., Frisk T. Thermal decomposition of ammonium paratungstate tetrahydrate under non-reducing conditions: Characterization by thermal analysis, X-ray diffraction and spectroscopic methods. *Thermochim. Acta*, 2008, **469**, P. 12–22.
[31] Hunyadi D., Sajó I., Szilágyi I.M. Structure and thermal decomposition of ammonium metatungstate. *J. Therm. Anal. Calorim.*, 2014, **116**, P. 329–337.
[32] Marafi M., Stanislaus A. Influence of catalyst acidity and feedstock quality on hydrotreating catalyst deactivation by coke deposition. *Pet. Sci. Technol.*, 2001, **19**, P. 697–710.
[33] Dychalska A., Popielarski P., Franków W., Fabisiak K., Paprocki K., Szybowicz M. Study of CVD diamond layers with amorphous carbon admixture by Raman scattering spectroscopy. *Mater. Sci.*, 2015, **33**.
[34] Guichard B., Roy-Auberger M., Devers E., Rebours B., Quoineaud A.A., Digne M. Characterization of aged hydrotreating catalysts. Part I: Coke depositions, study on the chemical nature and environment. *Appl. Catal. A Gen.*, 2009, **367**, P. 1–8.
[35] González-Cortés S.L., Qian Y., Almegren H.A., Xiao T., Kuznetsov V.L., Edwards P.P. Citric acid-assisted synthesis of γ-alumina-supported high loading CoMo sulfide catalysts for the hydrodesulfurization (HDS) and hydrodenitrogenation (HDN) reactions. *Appl. Petrochemical Res.*, 2015, **5**, P. 181–197.
[36] Tian H., Roberts C.A., Wachs I.E. Molecular Structural Determination of Molybdena in Different Environments: Aqueous Solutions, Bulk Mixed Oxides, and Supported MoO_3 Catalysts. *J. Phys. Chem. C*, 2010, **114**, P. 14110–14120.
[37] Goetze J., Meirer F., Yarulina I., Gascon J., Kapteijn F., Ruiz-Martínez J., Weckhuysen B.M. Insights into the Activity and Deactivation of the Methanol-to-Olefins Process over Different Small-Pore Zeolites As Studied with Operando UV-vis Spectroscopy. *ACS Catal.*, 2017, **7**, P. 4033–4046.
[38] Ross-Medgaarden E.I., Wachs I.E. Structural Determination of Bulk and Surface Tungsten Oxides with UV-vis Diffuse Reflectance Spectroscopy and Raman Spectroscopy. *J. Phys. Chem. C*, 2007, **111**, P. 15089–15099.
[39] Garbarino G., Riani P., Infantes-Molina A., Rodríguez-Castellón E., Busca G. On the detectability limits of nickel species on NiO/γ-Al_2O_3 catalytic materials. *Appl. Catal. A Gen.*, 2016, **525**, P. 180–189.
[40] Jeziorowski H., Knoezinger H. Raman and ultraviolet spectroscopic characterization of molybdena on alumina catalysts. *J. Phys. Chem.*, 1979, **83**, P. 1166–1173.
[41] da Silva V.L.S., Frety R., Schmal M. Activation and Regeneration of a NiMo/Al_2O_3 Hydrotreatment Catalyst. *Ind. Eng. Chem. Res.*, 1994, **33**, P. 1692–1699.
[42] Romanova T.S., Nadeina K.A., Danilova I.G., Danilevich V.V., Pakharukova V.P., Gabrienko A.A., Glazneva T.S., Gerasimov E.Y., Prosvirin I.P., Vatutina Y.V., Kazakov M.O., Klimov O.V., Noskov A.S. Modification of HDT catalysts of FCC feedstock by adding silica to the kneading paste of alumina support: Advantages and disadvantages. *Fuel*, 2022, **324**, 124555.
[43] Mohamed M.M., Ahmed S.A., Khairou K.S. Unprecedented high photocatalytic activity of nanocrystalline WO_3/$NiWO_4$ hetero-junction towards dye degradation: Effect of template and synthesis conditions. *Appl. Catal. B Environ.*, 2014, **150–151**, P. 63–73.
[44] Leonova K.A., Klimov O.V., Kochubey D.I., Chesalov Y.A., Gerasimov E.Y., Prosvirin I.P., Noskov A.S. Optimal pretreatment conditions for Co–Mo hydrotreatment catalysts prepared using ethylenediamine as a chelating agent. *Catal. Today*, 2014, **220–222**, P. 327–336.
[45] Bukhtiyarova G.A., Klimov O.V., Kochubey D.I., Noskov A.S., Pashigreva A.V. EXAFS study of oxide precursors of the high active Co–Mo hydrotreating catalysts: Effect of drying conditions. *Nucl. Instruments Methods Phys. Res. Sect. A Accel. Spectrometers, Detect. Assoc. Equip.*, 2009, **603**, P. 119–121.
[46] Courty P., Ajot H., Marcilly C., Delmon B. Oxydes mixtes ou en solution solide sous forme très divisée obtenus par décomposition thermique de précurseurs amorphes. *Powder Technol.*, 1973, **7**, P. 21–38.
[47] Leonova K.A., Klimov O.V., Kochubey D.I., Chesalov Y.A., Gerasimov E.Y., Prosvirin I.P., Noskov A.S. Optimal pretreatment conditions for Co–Mo hydrotreatment catalysts prepared using ethylenediamine as a chelating agent. *Catal. Today*, 2014, **220–222**, P. 327–336.
[48] Guzmán-Castillo M.L., Bokhimi X., Toledo-Antonio A., Salmones-Blásquez J., Hernández-Beltrán F. Effect of Boehmite Crystallite Size and Steaming on Alumina Properties. *J. Phys. Chem. B*, 2001, **105**, P. 2099–2106.
[49] Boumaza A., Favaro L., Lédion J., Sattonnay G., Brubach J.B., Berthet P., Huntz A.M., Roy P., Tétot R. Transition alumina phases induced by heat treatment of boehmite: An X-ray diffraction and infrared spectroscopy study. *J. Solid State Chem.*, 2009, **182**, P. 1171–1176.
[50] Liu Q., Wang A., Wang X., Zhang T. Mesoporous γ-alumina synthesized by hydro-carboxylic acid as structure-directing agent. *Microporous Mesoporous Mater.*, 2006, **92**, P. 10–21.
[51] Tichit D., El Alami D., Figueras F. Influence of the Preparation and of the Activation Treatments on the Catalytic Activity of Mechanical Mixtures of Sulfated Zirconia and Pt/Al_2O_3. *J. Catal.*,1996, **163**, P. 18–27.

[52] Ozkan U., Schrader G.L. $NiMoO_4$ selective oxidation catalysts containing excess MoO_3 for the conversion of C_4 hydrocarbons to maleic anhydride: I. Preparation and characterization. *J. Catal.*,1985, **95**, P. 120–136.
[53] Pampararo G., Garbarino G., Ardoino N., Riani P., Busca G. A study of molybdena catalysts in ethanol oxidation. Part 1. Unsupported and silica-supported MoO_3. *J. Chem. Technol. Biotechnol.*, 2021, **96**.
[54] Horsley J.A., Wachs I.E., Brown J.M., Via G.H., Hardcastle F.D. Structure of surface tungsten oxide species in the tungsten trioxide/alumina supported oxide system from x-ray absorption near-edge spectroscopy and Raman spectroscopy. *J. Phys. Chem.*, 1987, **91**, P. 4014–4020.
[55] Busca G. Differentiation of mono-oxo and polyoxo and of monomeric and polymeric vanadate, molybdate and tungstate species in metal oxide catalysts by IR and Raman spectroscopy. *J. Raman Spectrosc.*, 2002, **33**, P. 348–358.
[56] Mukhacheva P.P., Vatutina Y.V., Nadeina K.A., Budukva S.V., Panafidin M.A., Pakharukova V.P., Parfenov M.V., Gerasimov E.Y., Klimov O.V., Noskov A.S. Comparison of the HDS DBT Reaction Using Bulk and Supported Catalysts. *Chim. Techno Acta*, 2024, **11**, 202411206.
[57] Saih Y., Segawa K. Catalytic activity of CoMo catalysts supported on boron-modified alumina for the hydrodesulphurization of dibenzothiophene and 4.6-dimethyldibenzothiophene. *Appl. Catal. A Gen.*, 2009, **353**, P. 258–265.
[58] Okamoto Y., Nakano H., Shimokawa T., Imanaka T., Teranishi S. Stabilization effect of Co for Mo phase in Co-$MoAl_2O_3$ hydrodesulfurization catalysts studied with X-Ray photoelectron spectroscopy. *J. Catal.*, 1977, **50**, P. 447–454.
[59] Ben Tayeb K., Lamonier C., Lancelot C., Fournier M., Payen E., Bonduelle A., Bertoncini F. Study of the active phase of NiW hydrocracking sulfided catalysts obtained from an innovative heteropolyanion based preparation. *Catal. Today*, 2010, **150**, P. 207–212.
[60] Orsini G., Tricoli V. Facile nonhydrolytic sol–gel route to mesoporous mixed-conducting tungsten oxide. *J. Mater. Chem.*, 2011, **21**, P. 14530–14542.
[61] Lorenz M., Schulze M. XPS analysis of electrochemically oxidized nickel surfaces. *J. Anal. Chem.*, 1999, **365**, P. 154–157.
[62] Kazakova M.A., Kuznetsov V.L., Bokova-Sirosh S.N., Krasnikov D.V., Golubtsov G.V., Romanenko A.I., Prosvirin I.P., Ishchenko A.V., Orekhov A.S., Chuvilin A.L., Obraztsova E.D. Fe–Mo and Co–Mo Catalysts with Varying Composition for Multi-Walled Carbon Nanotube Growth. *Phys. Status Solidi*, 2018, **255**, 1700260.
[63] Klimov O.V., Nadeina K.A., Vatutina Y.V., Stolyarova E.A., Danilova I.G., Gerasimov E.Y., Prosvirin I.P., NoskovA.S. CoMo/Al_2O_3 hydrotreating catalysts of diesel fuel with improved hydrodenitrogenation activity. *Catal. Today*, 2018, **307**, P. 73–83.
[64] Bremmer G.M., van Haandel L., Hensen E.J.M., Frenken J.W.M., Kooyman P.J. The effect of oxidation and resulfidation on (Ni/Co)MoS_2 hydrodesulfurisation catalysts. *Appl. Catal. B Environ.*, 2019, **243**, P. 145–150.

Submitted 29 July 2024; revised 2 October 2024; accepted 7 November 2024

Information about the authors:

Ksenia A. Nadeina – Boreskov Institute of Catalysis SB RAS, Pr. Lavrentieva 5, 630090 Novosibirsk, Russia; ORCID 0000-0003-2671-5146; lakmallow@catalysis.ru

Yuliya V. Vatutina – Boreskov Institute of Catalysis SB RAS, Pr. Lavrentieva 5, 630090 Novosibirsk, Russia; ORCID 0000-0001-8898-9762; y.vatutina@catalysis.ru

Polina P. Mukhacheva – Boreskov Institute of Catalysis SB RAS, Pr. Lavrentieva 5, 630090 Novosibirsk, Russia; ORCID 0000-0002-5005-0781; mpp@catalysis.ru

Sergey V. Budukva – Boreskov Institute of Catalysis SB RAS, Pr. Lavrentieva 5, 630090 Novosibirsk, Russia; ORCID 0000-0001-7450-3960; zsm@catalysis.ru

Irina G. Danilova – Boreskov Institute of Catalysis SB RAS, Pr. Lavrentieva 5, 630090 Novosibirsk, Russia; ORCID 0000-0003-1476-9825; danig@catalysis.ru

Vera P. Pakharukova – Boreskov Institute of Catalysis SB RAS, Pr. Lavrentieva 5, 630090 Novosibirsk, Russia; ORCID 0000-0001-8808-0161; verapakharukova@yandex.ru

Evgeniy Yu. Gerasimov – Boreskov Institute of Catalysis SB RAS, Pr. Lavrentieva 5, 630090 Novosibirsk, Russia; ORCID 0000-0002-3230-3335; gerasimov@catalysis.ru

Maxim A. Panafidin – Boreskov Institute of Catalysis SB RAS, Pr. Lavrentieva 5, 630090 Novosibirsk, Russia; ORCID 0000-0001-6897-7692; mpanafidin@catalysis.ru

Oleg V. Klimov – Boreskov Institute of Catalysis SB RAS, Pr. Lavrentieva 5, 630090 Novosibirsk, Russia; ORCID 0000-0002-8089-2357; klm@catalysis.ru

Conflict of interest: the authors declare no conflict of interest.